

Learning complex nonlinear physical systems using wavelet neural operators

Yanan Guo(郭亚楠), Xiaoqun Cao(曹小群), Hongze Leng(冷洪泽), and Junqiang Song(宋君强)

Citation: Chin. Phys. B, 2025, 34 (**3**): 034702. DOI: 10.1088/1674-1056/ada7dc
Journal homepage: http://cpb.iphy.ac.cn; http://iopscience.iop.org/cpb

What follows is a list of articles you may be interested in

Bacterial turbulence in gradient confinement

Ningzhe Yan(颜宁哲), Chenliang Xie(谢晨亮), Hao Luo(罗昊), Yanan Liu(刘亚楠), and Guangyin Jing(经光银)
Chin. Phys. B, 2023, 32 (**11**): 114704. DOI: 10.1088/1674-1056/acea6d

Computational and experimental investigations of a microfluidic mixer for efficient iodine extraction using carbon tetrachloride enhanced with gas bubbles

Siddique Muhammad Kashif, Sun Lin(孙林), and Li Songjing(李松晶)
Chin. Phys. B, 2023, 32 (**11**): 114702. DOI: 10.1088/1674-1056/acf03f

Dynamic evolution of low-viscosity fuel particle distribution driven by constant flow

Zhong-Kun Yang(杨仲坤), Gao-Jun An(安高军), Xi-Meng Xu(徐曦萌), Zhe Zheng(郑哲), Yong-Xu Wang(王永旭), Li-Feng Xie(解立峰), Dan Zhang(张丹), and Bin Li(李斌)
Chin. Phys. B, 2023, 32 (**7**): 074701. DOI: 10.1088/1674-1056/acc8c2

Numerical simulation of the thermal non-equilibrium flow-field characteristics of a hypersonic Apollo-like vehicle

Minghao Yu(喻明浩)†, Zeyang Qiu(邱泽洋), Bo Lv(吕博), and Zhe Wang(王哲)

Chin. Phys. B, 2022, 31 (**9**): 094702. DOI: 10.1088/1674-1056/ac6ed6 Shedding vortex simulation method based on viscous compensation technology research

Hao Zhou(周昊), Lei Wang(汪雷), Zhang-Feng Huang(黄章峰), and Jing-Zhi Ren(任晶志)
Chin. Phys. B, 2022, 31 (**4**): 044702. DOI: 10.1088/1674-1056/ac29ae

---

Learning complex nonlinear physical systems using wavelet neural operators

Yanan Guo(郭亚楠)[1,2,3], Xiaoqun Cao(曹小群)[1,†], Hongze Leng(冷洪泽)[1], and Junqiang Song(宋君强)[1]

[1] *College of Meteorology and Oceanography, National University of Defense Technology, Changsha* 410073, *China*
[2] *College of Computer, National University of Defense Technology, Changsha* 410073, *China*
[3] *Naval Aviation University, Huludao* 125001, *China*

(Received 1 December 2024; revised manuscript received 2 January 2025; accepted manuscript online 9 January 2025)

Nonlinear science is a fundamental area of physics research that investigates complex dynamical systems which are often characterized by high sensitivity and nonlinear behaviors. Numerical simulations play a pivotal role in nonlinear science, serving as a critical tool for revealing the underlying principles governing these systems. In addition, they play a crucial role in accelerating progress across various fields, such as climate modeling, weather forecasting, and fluid dynamics. However, their high computational cost limits their application in high-precision or long-duration simulations. In this study, we propose a novel data-driven approach for simulating complex physical systems, particularly turbulent phenomena. Specifically, we develop an efficient surrogate model based on the wavelet neural operator (WNO). Experimental results demonstrate that the enhanced WNO model can accurately simulate small-scale turbulent flows while using lower computational costs. In simulations of complex physical fields, the improved WNO model outperforms established deep learning models, such as U-Net, ResNet, and the Fourier neural operator (FNO), in terms of accuracy. Notably, the improved WNO model exhibits exceptional generalization capabilities, maintaining stable performance across a wide range of initial conditions and high-resolution scenarios without retraining. This study highlights the significant potential of the enhanced WNO model for simulating complex physical systems, providing strong evidence to support the development of more efficient, scalable, and high-precision simulation techniques.

Keywords: nonlinear science, turbulence, deep learning, wavelet neural operator

PACS: 47.27.E–, 02.60.Cb, 07.05.Mh, 02.30.Jr

DOI: 10.1088/1674-1056/ada7dc **CSTR:** 32038.14.CPB.ada7dc

1. Introduction

Complex nonlinear phenomena typically involve multi-scale interactions, ranging from microscopic vortices to large-scale atmospheric circulations. The governing equations for these phenomena are often represented by highly nonlinear partial differential equations (PDEs).[1–3] High-precision simulation of such complex nonlinear phenomena not only deepens our understanding of the Earth system but also provides critical support for addressing global challenges, including climate change, natural disasters, and sustainable resource management.[4,5] However, achieving high-precision solutions to nonlinear PDEs poses significant computational challenges. Traditional methods, such as direct numerical simulation (DNS) and large eddy simulation (LES), often incur prohibitively high costs for long-duration or high-fidelity simulations.[6–9] While DNS offers unparalleled accuracy by resolving all turbulent scales, its computational cost escalates dramatically with increasing Reynolds numbers and spatial dimensions, severely limiting its applicability.[10,11] LES alleviates this burden by modeling small-scale structures, but it still requires substantial computational resources and may struggle to capture subtle features critical in certain applications.

To address the high cost and complexity of traditional simulation frameworks, recent years have seen rapid advancements in data-driven simulation methods. These approaches leverage large volumes of experimental or simulation data to develop surrogate models capable of predicting the evolution of complex physical systems without explicitly solving complex PDEs at each time step.[12–18] deep learning (DL) models, such as convolutional neural networks (CNNs) and recurrent neural networks (RNNs), have demonstrated remarkable abilities in capturing complex nonlinear dynamics and subtle spatiotemporal correlations.[19–22] Specifically, CNNs excel at extracting spatial features, while architectures like long short-term memory networks are adept at modeling temporal dependencies, enabling more accurate predictions of turbulence, vortex dynamics, and other key fluid phenomena.

Despite these advancements, traditional DL methods are often limited by their dependence on specific discretizations or parameter ranges, restricting their ability to generalize to new scenarios. When physical conditions, resolutions, or computational grids change, expensive retraining is typically required. Additionally, these methods generally require large training datasets, which can be costly or difficult to obtain, especially

†Corresponding author. E-mail: caoxiaoqun@nudt.edu.cn

© 2025 Chinese Physical Society and IOP Publishing Ltd. All rights, including for text and data mining, AI training, and similar technologies, are reserved.

for rare or highly complex flow events. These limitations have driven the development of more flexible frameworks capable of learning mappings between function spaces without relying on fixed discretizations.

Neural operators have recently emerged as a promising paradigm for directly learning operators from data, such as integral transforms or solution mappings of PDEs.[23,24] Unlike traditional neural networks optimized for specific grids or resolutions, neural operators aim to approximate function mappings independent of discretization, enabling generalization across various discretizations and problem settings. Among these approaches, the Fourier neural operator (FNO) has attracted significant attention due to its ability to learn PDE solution operators in the spectral domain using Fourier transforms.[25–27] FNO excels in modeling complex fluid dynamic scenarios, including turbulence, by providing a computationally efficient alternative that maintains high accuracy while reducing training and inference costs.[28–30]

However, FNO-based methods may struggle to capture certain local small-scale features and adapt to the wide range of scales encountered in real-world physical scenarios. To address these challenges, researchers have proposed the wavelet neural operator (WNO),[31,32] which decomposes signals into multiresolution components using wavelet transforms. Wavelets have compact support and the ability to simultaneously represent both local and global features, providing strong support for capturing the heterogeneity and multiscale characteristics of turbulence. By parameterizing operators in the wavelet domain, WNO can effectively encode both large-scale features and detailed information. Therefore, compared to previous methods, WNO offers higher accuracy, adaptability, and computational efficiency.

In this study, we introduce a novel WNO-based surrogate modeling approach for complex turbulent flow phenomena. Our results demonstrate that the enhanced WNO framework achieves orders of magnitude reduction in computational costs compared to traditional DNS and LES methods without compromising accuracy. Furthermore, the enhanced WNO model outperforms state-of-the-art deep learning models, such as UNet, ResNet, and FNO, in capturing small-scale turbulent motions while maintaining excellent generalization capabilities. This includes robust performance under varying initial conditions and high-resolution scenarios without the need for retraining. These findings highlight the potential of WNO as a transformative tool for fluid simulation, paving the way for more scalable, efficient, and versatile modeling paradigms that meet the growing demands of scientific and engineering applications.

2. Methodology

In this paper, we investigate operator mappings between infinite-dimensional function spaces. Specifically, we consider an operator $\mathcal{D}: A \to U$, where A and U are appropriately chosen function spaces defined on a domain $D \subseteq \mathbb{R}^n$. Here, A represents spaces of input fields, such as source terms, initial conditions, and boundary conditions in the context of PDEs, while U denotes the corresponding solution space of PDEs on D. Our objective is to approximate the operator $\mathcal{D}$ using a neural network parameterized by θ_{NN}, specifically aiming to learn an approximation $\mathcal{D}_{\theta_{\mathrm{NN}}}$. In particular, we focus on the wavelet neural operator introduced in Ref. [31], which leverages wavelet transforms to achieve efficient, resolution-invariant representations of complex spatiotemporal dynamics.

To train such an operator, we first discretize the domain D into n_D grid points and construct a dataset $\{(a_j, u_j)\}_{j=1}^{N} \subset A \times U$, where each a_j represents an input field and u_j denotes the corresponding PDE solution. The training process begins by applying a lifting operator $P: A \to \mathbb{R}^{n_D \times d_v}$ to map the input field $a(x)$ to a higher-dimensional representation $v_0(x)$. Subsequently, we perform iterative updates using a parameterized kernel integral operator $\mathcal{K}(a;\phi)$ to generate intermediate representations $v_j(x)$. In the wavelet neural operator framework, the kernel function is parameterized not directly in the physical domain but in the wavelet domain, thereby taking advantage of the multi-scale and localized properties of wavelet bases.

Since directly applying the continuous wavelet transform is less efficient and not well-defined for discrete domains, we instead employ the discrete wavelet transform (DWT). The DWT is particularly well-suited for discrete data, providing a hierarchical, multi-scale representation of signals that captures localized features in both space and frequency. We utilize Daubechies wavelets due to their compact support, orthogonality, and ability to form a stable, orthonormal basis for $L^2(\mathbb{R})$. These properties ensure that any function with appropriate regularity in $L^2(\mathbb{R})$ can be represented as a series expansion in terms of Daubechies wavelets, thereby facilitating both analysis and synthesis.

In the WNO framework, the input data $v_j \in \mathbb{R}^{n_D \times d_v}$ is first transformed into the wavelet domain via W, the DWT operator, and then processed by a parameterized kernel function R_ϕ, which acts multiplicatively on the wavelet coefficients. Let W^{-1} denote the inverse DWT; we then express the integral operator in the wavelet domain as

$$(K(\phi) * v_j)(x) = W^{-1}\big(R_\phi \cdot W(v_j)\big)(x). \tag{1}$$

Here $R_\phi = W(k_\phi)$ denotes the kernel function k_ϕ projected into the wavelet domain. By parameterizing the kernel function, we can capture the dominant behavior of the PDE solutions,

specifically the low-frequency (global) components. Simultaneously, by incorporating additional details from lower scales (high-frequency components), we can accurately extract local structures and non-stationarities in the data. This hierarchical approach reduces computational complexity while preserving essential information.

Let $\psi(x) \in L^2(\mathbb{R})$ be an orthogonal mother wavelet. The set $\{\psi_{m,\tau}(x)\}$, defined by $\psi_{m,\tau}(x) = 2^{-m/2}\psi\left(\frac{x-\tau}{2^m}\right)$, forms a complete orthonormal basis of $L^2(\mathbb{R})$ under appropriate conditions. For a function $\Gamma : D \to \mathbb{R}^{d_v}$, its DWT and inverse DWT can be expressed as

$$\begin{aligned}(W\Gamma)_j(m,\tau) &= \frac{1}{\sqrt{2^m}}\int_D \Gamma(x)\,\psi\left(\frac{x-\tau}{2^m}\right)\mathrm{d}x,\\ (W^{-1}\Gamma_w)_j(x) &= \sum_{m,\tau}(\Gamma_w)_j(m,\tau)\,\psi_{m,\tau}(x),\end{aligned} \tag{2}$$

where $j \in \{1,\ldots,d_v\}$ indexes the feature dimension, and $m,\tau \in \mathbb{Z}$ index the scale and translation parameters, respectively. In practice, when implemented via filter banks, these continuous integrals and sums correspond to discrete convolutions and downsamplings, ensuring computational efficiency.

By leveraging the properties of the wavelet transform, the operator can be expressed as

$$(K(\phi) * v_j)(x) = W^{-1}\big(W(k_\phi)\cdot W(v_j)\big)(x), \quad x \in D. \tag{3}$$

Since $R_\phi = W(k_\phi)$, we obtain

$$(K(\phi) * v_j)(x) = W^{-1}\big(R_\phi \cdot W(v_j)\big)(x), \quad x \in D. \tag{4}$$

To implement the parameterization, we represent R_ϕ as a weight tensor $R \in \mathbb{R}^{\zeta\times d_v\times d_v}$, where ζ denotes the number of retained wavelet coefficients at a given scale level. Let $W(v_{j,m}) \in \mathbb{R}^{\zeta\times d_v}$ represent the wavelet coefficients of v_j at scale m. The convolution-like operation in the wavelet domain is then given by

$$(R\cdot W(v_{j,m}))_{I_1,I_2} = \sum_{I_3=1}^{d_v} R_{I_1,I_2,I_3}\,W(v_{j,m})_{I_1,I_3}. \tag{5}$$

After discretizing the domain and obtaining high-dimensional fields, the WNO employs multi-level wavelet decomposition to achieve dimensionality reduction and efficient learning. At each scale m, we perform the necessary operations in the wavelet domain, then apply W^{-1} to map back, ensuring that learned parameters at higher scales hierarchically propagate information to finer scales. This inherently multi-resolution scheme facilitates compact representations and the systematic integration of both global and local information.

The overall WNO architecture, schematically depicted in Fig. 1, comprises three primary components: a lifting layer $P(\cdot)$ that maps the input $a(x) \in A$ to a suitable high-dimensional feature space, multiple wavelet kernel layers $K(\cdot)$ that apply integral transforms in the wavelet domain and a projection layer $Q(\cdot)$ that maps the final representation to the solution space $u(x) \in U$. Nonlinear activation functions may be employed after the projection to enhance representational capacity. Compared with the FNO, the WNO leverages wavelets' localized basis functions and multi-scale decomposition, enabling a more effective representation of non-stationary phenomena and complex local structures commonly present in PDE solutions.

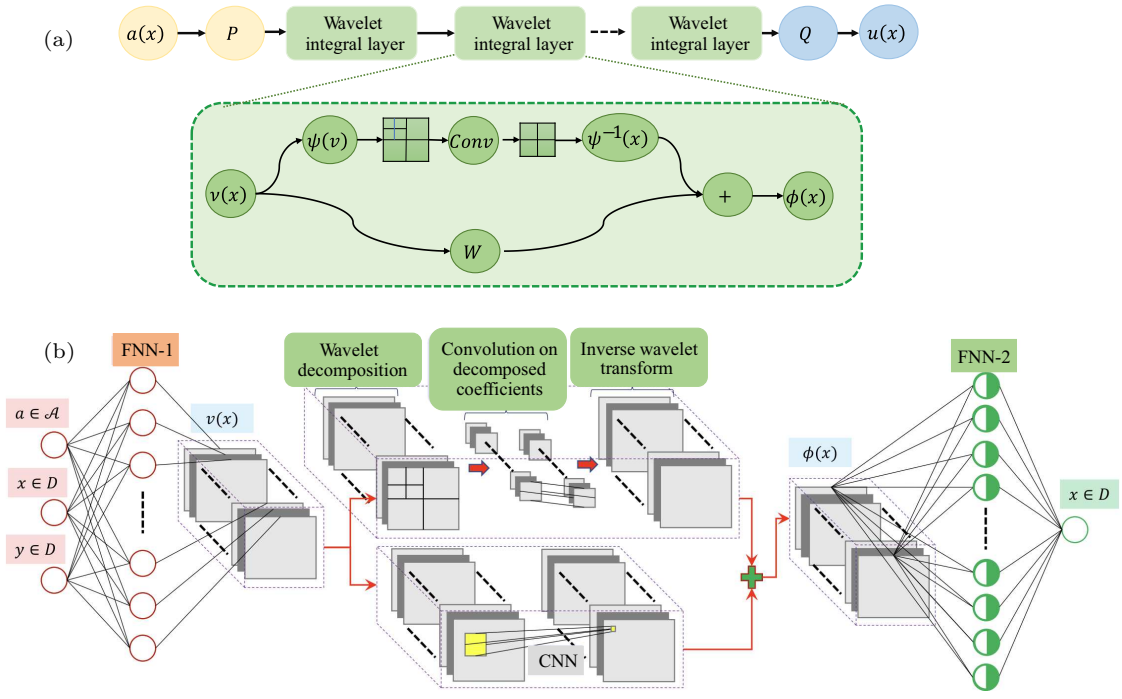


Fig. 1. Schematic of the wavelet neural operator architecture.

By introducing wavelet transforms, the WNO can accurately model highly nonlinear differential operators without the need for specific geometric structures. However, the WNO has certain limitations in extracting high-frequency information from the data. In contrast, U-Net excels at performing local convolution operations and preserves more detailed information by directly passing feature maps from the encoder to the decoder. Therefore, integrating the U-Net framework enhances the WNO's ability to analyze and predict high-frequency features. U-Net downsamples the data to different scales, enabling convolution operations at multiple levels to capture high-frequency information.

To further enhance the performance of each wavelet layer, we introduce residual skip connections. These residual connections ensure efficient information transfer between layers, preventing issues such as vanishing gradients or information loss, thereby improving the neural operator's learning capability in the spatial domain. In each wavelet layer, the relationship between the input and output is defined as follows:
For $j = 0$,

$$v_{j+1}(x) := \sigma\left(na(Kv_j)(x) + W(v_j(x))\right). \tag{6}$$

For $j = 1, 2, \ldots, L$,

$$\begin{aligned} v_{j+1}(x) :=\ & \sigma\left(na(K(v_j + v_0))(x) + W(v_j(x)) + U(v_j(x))\right), \\ & \forall x \in D, \end{aligned} \tag{7}$$

where K represents the kernel integral transform, W is the learnable linear operator, σ denotes the nonlinear adaptive activation function, and U corresponds to the CNN operator within the U-Net framework. The convolution kernel sizes used in the U-Net path differ from those in W, facilitating the extraction of richer features across multiple scales and thereby enhancing feature representation capabilities.

The design of the enhanced WNO architecture involves three main steps. First, similar to the WNO, the input function $a(x)$ is mapped to a higher-dimensional space as follows:

$$v_0(x) = P(a(x)). \tag{8}$$

Next, the U-WNO layers are applied sequentially

$$v_0 \to v_1 \to \cdots \to v_L, \tag{9}$$

where v_j denotes the output of the j-th layer ($j = 0, 1, \ldots, L$). Finally, after passing through L layers, v_L is projected back into the original space to produce the final output

$$u(x) = Q(v_L(x)). \tag{10}$$

U-WNO effectively combines the multi-scale characteristics of wavelet transforms with the powerful feature extraction capabilities of U-Net. This integration not only enables more effective analysis and prediction of high-frequency information, but also significantly enhances the expressiveness and predictive power of the neural operator in complex scenarios.

Additionally, we have incorporated a self-attention mechanism. The core idea of self-attention is to allow the model to leverage information from different locations by automatically learning the relationships and significance between various positions in the input sequence. This approach addresses a key limitation of traditional RNNs and CNNs, which typically focus only on local information. Consider three sequences, Q, K, and V, defined as follows:

$$\begin{aligned} Q &= \mathrm{DET}_m \times W_Q, \\ K &= \mathrm{DET}_m \times W_K, \\ V &= \mathrm{DET}_m \times W_V, \end{aligned} \tag{11}$$

where W_Q, W_K, and W_V are learnable parameter matrices that define the attention mechanism. The attention mechanism is computed as

$$\mathrm{Attention}(Q, K, V) = \mathrm{softmax}\left(\frac{QK^{\mathrm{T}}}{\sqrt{d_k}}\right)V. \tag{12}$$

By combining Eqs. (11) and (12), we can compute the updated detail coefficients DET'_m as follows:

$$\mathrm{DET}'_m = \mathrm{Attention}(Q, K, V). \tag{13}$$

The self-attention mechanism is incorporated into the WNO framework using the previously described procedures. Specifically, the input signal is decomposed into (m) levels using the DWT, with each decomposition yielding a pair of approximation coefficients and detail coefficients. The detail coefficients capture high-frequency features, while the approximation coefficients contain low-frequency components. Generally, the high-frequency signals at the lower levels tend to be dominated by noise. In comparison, the wavelet coefficients at the higher levels encapsulate the most critical information in the signal. By applying the self-attention mechanism to the detail coefficients DET_m in the m-th layer of the wavelet domain, we can capture the relationship between these coefficients, thus enhancing the neural network's ability to model complex flow fields.

3. Numerical experiments and results

3.1. Incompressible Boussinesq turbulence model

3.1.1. Experimental setup and dataset

This study systematically evaluates the potential of the enhanced WNO model in simulating turbulent entrainment-mixing processes.[33,34] High-resolution particle-resolved direct numerical simulation (PR-DNS) data were utilized as benchmark data to train the enhanced WNO model, thereby

constructing an efficient surrogate model capable of performing meaningful turbulence simulations. To generate the training data, we employed the PR-DNS model developed by Gao *et al.*,[35] which is based on an incompressible Boussinesq fluid framework, as described below:

$$\frac{\partial \boldsymbol{u}}{\partial t}+(\boldsymbol{u}\cdot\nabla)\boldsymbol{u}=-\frac{1}{\rho_0}\nabla p+\nu\nabla^2\boldsymbol{u}+\boldsymbol{f}_{\rm b}+\boldsymbol{f}_{\rm e}, \tag{14}$$

$$\nabla\cdot\boldsymbol{u}=0, \tag{15}$$

where $\boldsymbol{u}$ represents the fluid velocity field, p denotes the pressure, ν is the kinematic viscosity, and ρ_0 is the density of dry air. The buoyancy term $\boldsymbol{f}_{\rm b}$ in Eq. (14) is given by

$$\boldsymbol{f}_{\rm b}=-\left(\frac{T-T_0}{T_0}+0.608(q_{\rm v}-q_{\rm v0})-q_{\rm c}\right)\boldsymbol{g}, \tag{16}$$

where $\boldsymbol{g}$ represents the gravitational acceleration vector, T is the temperature, $q_{\rm v}$ is the water vapor mixing ratio, $q_{\rm c}$ is the liquid water mixing ratio, and T_0 and $q_{\rm v0}$ are reference values. The buoyancy term $\boldsymbol{f}_{\rm b}$ couples the velocity equation with the temperature and water vapor equations, thereby capturing the interactions among fluid velocity, temperature, water vapor mixing ratio, and the microphysical processes in cloud dynamics. Additionally, the external force $\boldsymbol{f}_{\rm e}$ in Eq. (14) is introduced to maintain a statistically stable turbulent state.

$$\frac{\partial T}{\partial t}+(\boldsymbol{u}\cdot\nabla)T=\frac{L_{\rm h}}{c_p}C_{\rm d}+\kappa_T\nabla^2T, \tag{17}$$

$$\frac{\partial q_{\rm v}}{\partial t}+(\boldsymbol{u}\cdot\nabla)q_{\rm v}=-C_{\rm d}+D_{\rm v}\nabla^2q_{\rm v}, \tag{18}$$

where $L_{\rm h}$ represents the latent heat of condensation, c_p is the specific heat capacity at constant pressure, κ_T is the thermal diffusivity, and $D_{\rm v}$ denotes the molecular diffusivity of water vapor. The condensation rate $C_{\rm d}$ is a function of the droplet radius $R_i(t)$, which establishes the coupling between the Lagrangian particles and the Eulerian field. This relationship is given by

$$C_{\rm d}(\boldsymbol{X},t)=\frac{4\pi\rho_{\rm l}A}{\rho_0a^3}\sum_{i=1}^{n}S(\boldsymbol{X}_i,t)R_i(t). \tag{19}$$

Here a represents the grid cell size, n is the number of droplets within the grid cell, $\rho_{\rm l}$ and ρ_0 are the densities of liquid water and air, respectively, and $R_i(t)$ is the radius of the i-th droplet. The condensation rate $C_{\rm d}$ serves as a source term in Eqs. (17) and (18), thereby coupling the particle dynamics with the fluid dynamics model. The function A depends on temperature and pressure and is expressed as

$$A=\left[\left(\frac{L_{\rm h}}{R_{\rm v}T}-1\right)\frac{L_{\rm h}\rho_{\rm l}}{k_TT}+\frac{\rho_{\rm l}R_{\rm v}T}{D_{\rm v}e_{\rm s}(T)}\right]^{-1} \tag{20}$$

where $R_{\rm v}=461.5\ {\rm J\cdot kg^{-1}\cdot K^{-1}}$ is the gas constant for water vapor, $e_{\rm s}(T)$ is the saturation vapor pressure, $\rho_{\rm l}$ is the liquid water density, k_T is the thermal conductivity of air, and $D_{\rm v}$ is the molecular diffusivity of water vapor. The supersaturation $S(\boldsymbol{X},t)$ is computed from the water vapor mixing ratio $q_{\rm v}(\boldsymbol{X},t)$ and the corresponding saturation water vapor mixing ratio $q_{\rm v,s}(\boldsymbol{X},t)$ as follows:

$$S(\boldsymbol{X},t)=\frac{q_{\rm v}(\boldsymbol{X},t)}{q_{\rm v,s}(\boldsymbol{X},t)}-1. \tag{21}$$

The equations governing the motion and evolution of the droplets are given by

$$\frac{{\rm d}\boldsymbol{X}_i(t)}{{\rm d}t}=\boldsymbol{V}_i(t), \tag{22}$$

$$\frac{{\rm d}\boldsymbol{V}_i(t)}{{\rm d}t}=\frac{1}{\tau_{\rm p}}[\boldsymbol{u}(\boldsymbol{X}_i,t)-\boldsymbol{V}_i(t)]+\boldsymbol{g}, \tag{23}$$

$$R_i(t)\frac{{\rm d}R_i(t)}{{\rm d}t}=A\cdot S(\boldsymbol{X}_i,t). \tag{24}$$

Here $R_i(t)$, $\boldsymbol{X}_i(t)$, and $\boldsymbol{V}_i(t)$ represent the radius, position, and velocity of the i-th droplet at time t, respectively. Equation (22) describes the droplet motion, while equation (23) defines the particle response time $\tau_{\rm p}$, which is given by

$$\tau_{\rm p}=\frac{2\rho_{\rm l}R_i^2}{9\rho_0\nu}. \tag{25}$$

Here, $\rho_{\rm l}$ and ρ_0 denote the densities of liquid water and dry air, respectively, R_i signifies the radius of the droplet, and ν represents the kinematic viscosity of air. Equation (25), derived from Stokes' law, applies to droplets with radii smaller than the Kolmogorov scale, which is the characteristic length scale of the smallest turbulent structures within a flow.[36] Under low Reynolds number conditions, the motion of the droplets is primarily governed by viscous drag, with inertial forces playing a negligible role. The gravitational force, denoted by $\boldsymbol{g}$, accounts for the settling velocity of the droplets under the influence of gravity.

For the simulations, the computational domain was set to $0.512\ {\rm m}\times0.512\ {\rm m}$, with periodic boundary conditions applied in the two-dimensional space. PR-DNS simulations were conducted on grids of sizes 64×64, 128×128, and 256×256, corresponding to grid spacings of 8 mm, 4 mm, and 2 mm, respectively. Additionally, simulations were performed on the 128×128 grid with varying initial conditions to assess the robustness of the deep learning model. The time step was set to an average of 0.003 s, ensuring that the Courant–Friedrichs–Lewy condition was satisfied. The initial Reynolds number was 6827, and the Rayleigh number was 40227. This simulation framework effectively captures the small-scale dynamics of turbulence and its interaction with cloud droplets, providing valuable insights into gas–liquid interactions in atmospheric turbulence. Furthermore, it generates crucial data for the application of deep learning models in turbulence simulations.

3.1.2. Experimental results

In this research, we initially trained an enhanced wavelet neural operator model using high-fidelity particle-resolved direct numerical simulation data and conducted prediction experiments to evaluate its performance in accurately forecasting velocity and temperature fields. To rigorously assess the model's accuracy and robustness, we compared the enhanced WNO's predictions with PR-DNS reference solutions and generated error distribution maps at various time points to quantify the deviations between the model's outputs and actual data.

The experimental outcomes demonstrate the enhanced WNO model's exceptional capability in capturing critical flow features. Specifically, at a resolution of 64×64, the model precisely predicts the X-velocity and temperature fields, closely matching the true data. The model successfully reproduced key characteristics of the flow, including regions with sharp velocity gradients. As shown in Fig. 2, the error distribution maps indicate that prediction errors are largely confined to a small range and are minimal, highlighting the model's ability to accurately replicate complex turbulent structures. Although a slight increase in error is observed in regions of intense turbulence, the overall error magnitude remains low, confirming the enhanced WNO's robustness and precision.

Notably, the enhanced WNO demonstrates a robust capability in accurately predicting the temperature field, with its spatial distribution exhibiting excellent agreement with the reference PR-DNS data. As depicted in Fig. 3, the error maps indicate marginally elevated errors in the vicinity of the boundary layers, which can likely be attributed to the presence of complex small-scale structures within the temperature field. Nonetheless, the overall error remains negligible, thereby further substantiating the enhanced WNO's proficiency in achieving high-fidelity simulations of both velocity and temperature fields.

To comprehensively evaluate the scalability and computational capability of the enhanced WNO model in resolving finer flow details, we increased the simulation resolution to 128×128. At this elevated resolution, the model successfully captures complex flow structures and subtle temperature variations, with partial results illustrated in Figs. 4 and 5. Although a marginal increase in error is observed in localized regions, the errors remain negligible. This outcome fully demonstrates the enhanced WNO's ability to maintain robust predictive accuracy and stability, even under the more demanding conditions of higher resolution simulations.

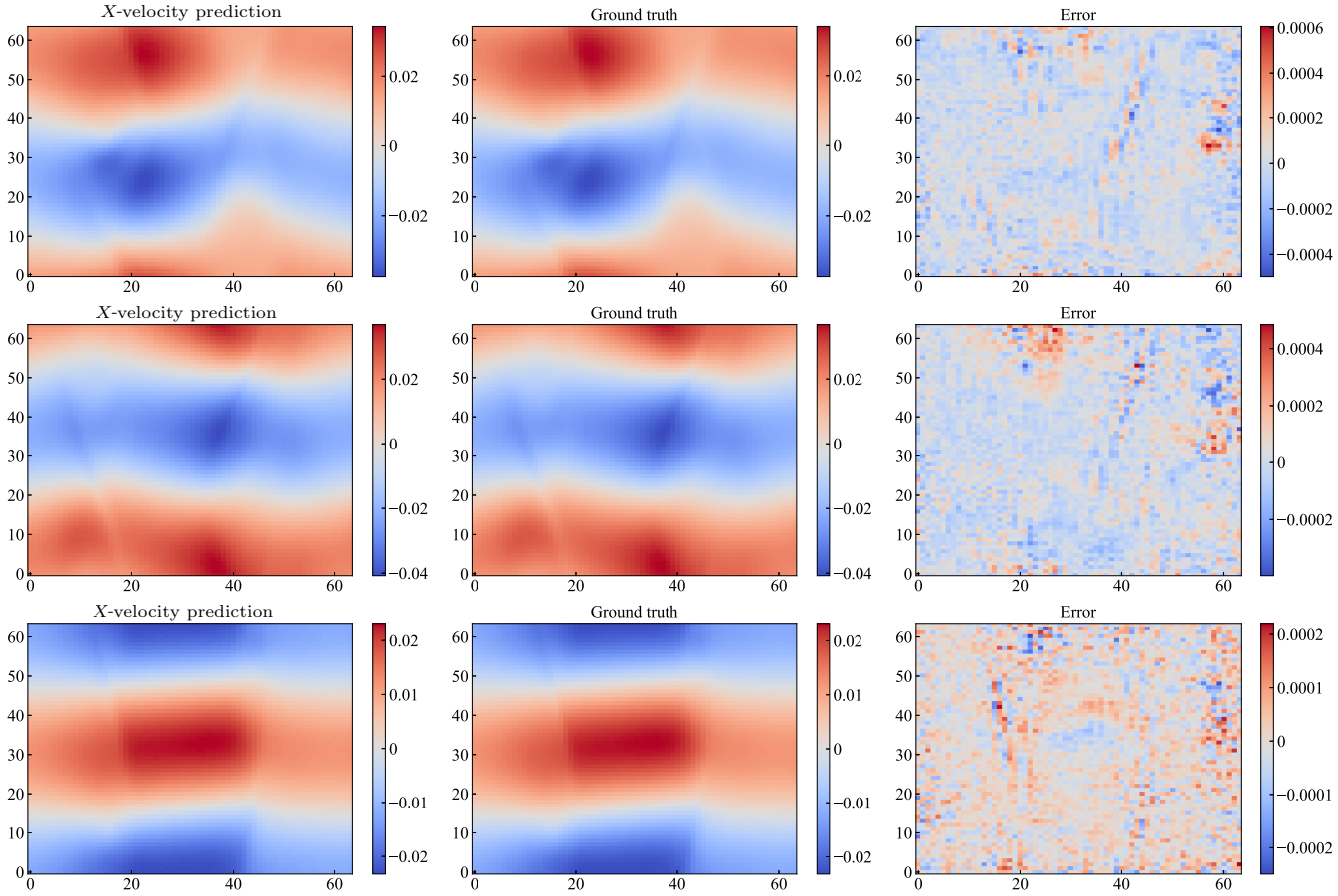


Fig. 2. Snapshot prediction of X-velocity by the enhanced WNO (left column), ground truth (middle column), and error distribution (right column) at three different time steps with a resolution of 64×64.

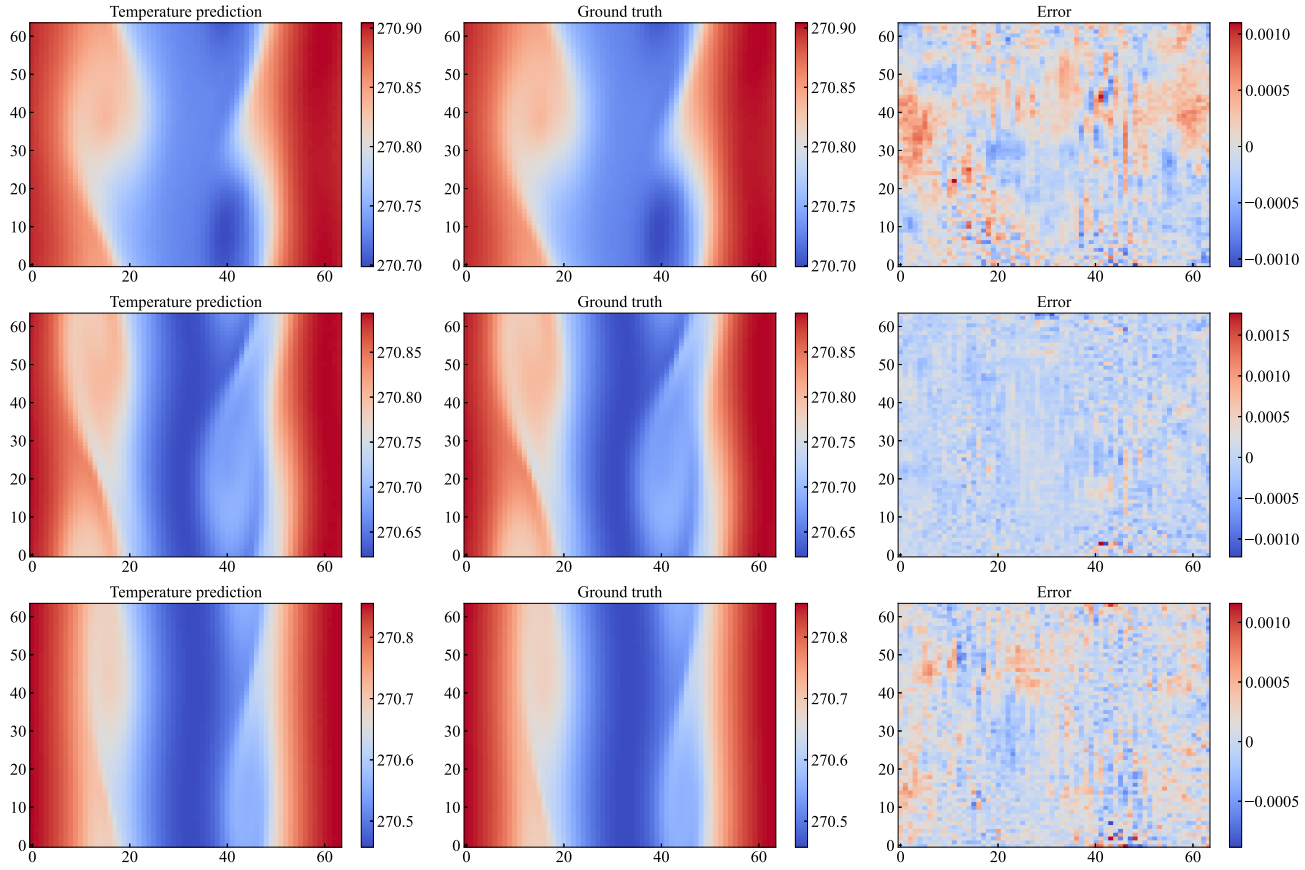


Fig. 3. Snapshot prediction of temperature by the enhanced WNO (left column), ground truth (middle column), and error distribution (right column) at three different time steps with a resolution of 64×64.

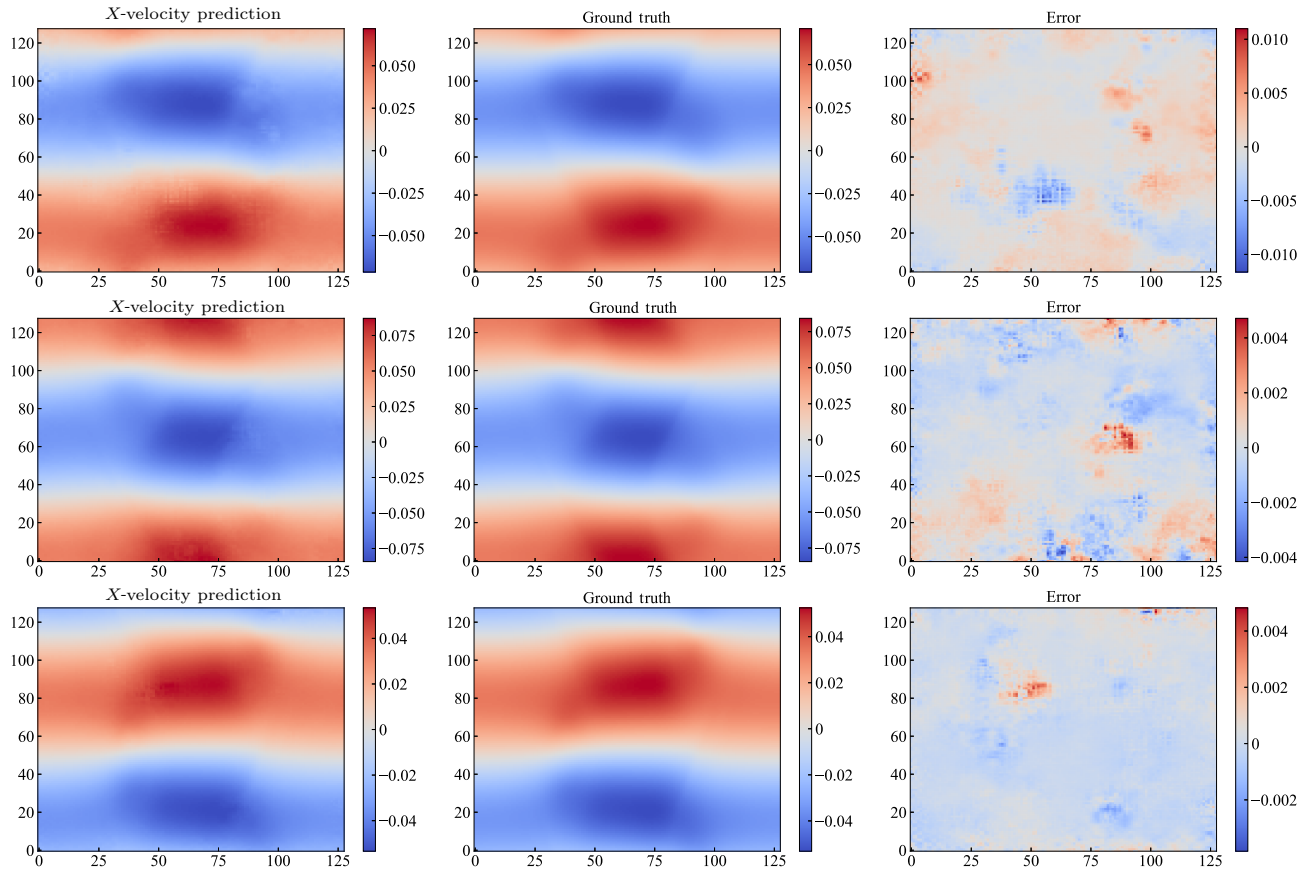


Fig. 4. Snapshot prediction of X-velocity by the enhanced WNO (left column), ground truth (middle column), and error distribution (right column) at three different time steps with a resolution of 128×128.

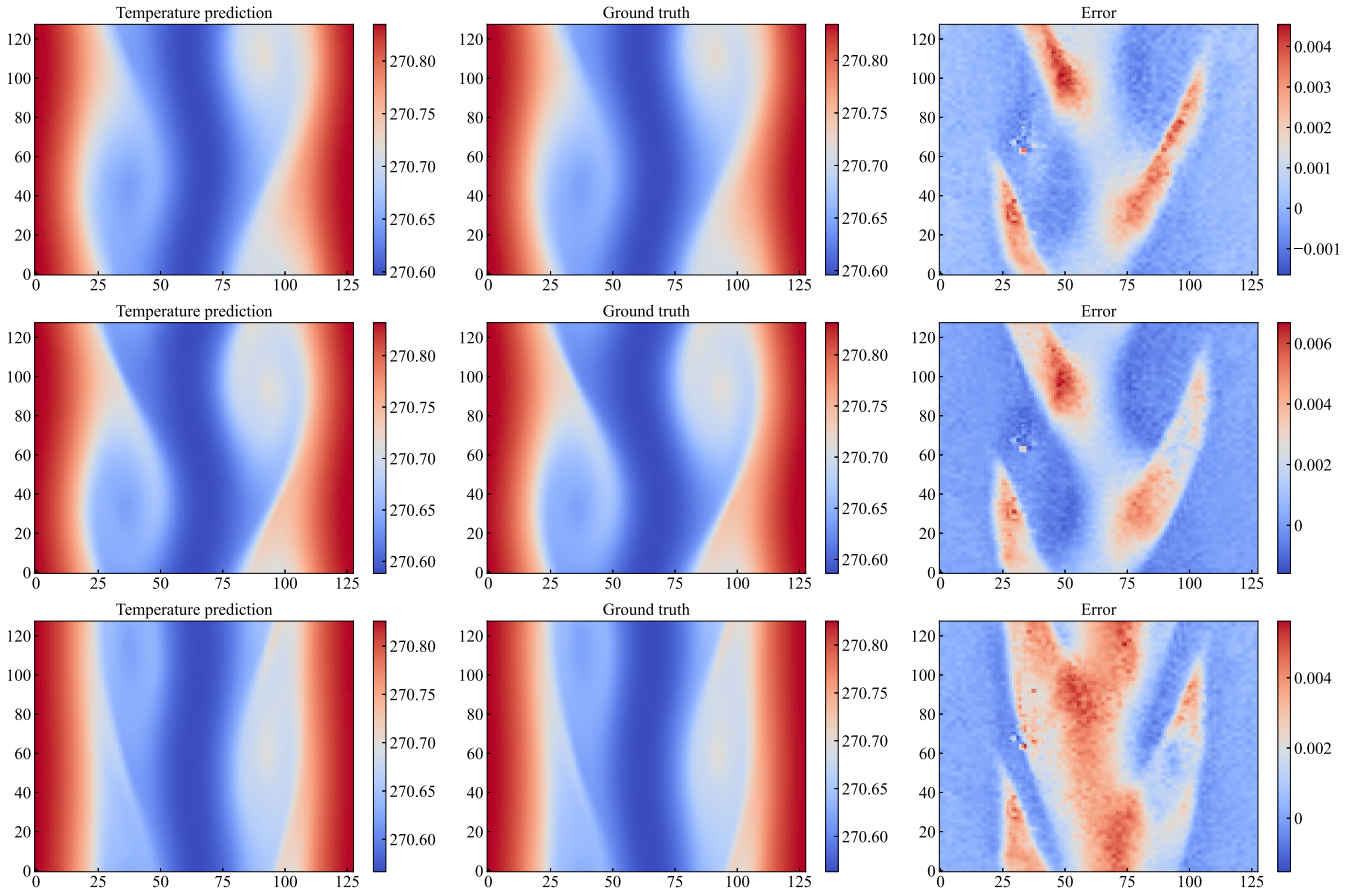


Fig. 5. Snapshot prediction of temperature by the enhanced WNO (left column), ground truth (middle column), and error distribution (right column) at three different time steps with a resolution of 128×128.

Table 1. Comparative analysis of $L2$ error metrics for X-velocity across different models at multiple resolutions: 64×64, 128×128, and 256×256.

Models	**64×64**	**128×128**	**256×256**
UNet	9.83×10^{-2}	6.14×10^{-2}	8.52×10^{-2}
ResNet	3.57×10^{-3}	3.80×10^{-3}	4.27×10^{-3}
FNO	5.86×10^{-4}	8.49×10^{-4}	7.90×10^{-4}
The enhanced WNO	$\mathbf{1.05 \times 10^{-4}}$	$\mathbf{1.86 \times 10^{-4}}$	$\mathbf{1.53 \times 10^{-4}}$

Table 2. Comparative analysis of $L2$ error metrics for temperature across different models at multiple resolutions: 64×64, 128×128, and 256×256.

Models	**64×64**	**128×128**	**256×256**
UNet	8.59×10^{-1}	9.24×10^{-1}	9.80×10^{-1}
ResNet	4.57×10^{-2}	7.69×10^{-2}	9.22×10^{-2}
FNO	9.60×10^{-3}	4.83×10^{-2}	1.05×10^{-1}
The enhanced WNO	$\mathbf{2.40 \times 10^{-3}}$	$\mathbf{3.05 \times 10^{-2}}$	$\mathbf{4.95 \times 10^{-2}}$

Furthermore, we conducted experimental validation of the model's performance at a resolution of 256×256 and systematically compared the $L2$ error metrics of the enhanced WNO model with those of UNet, ResNet, and FNO at resolutions of 64×64, 128×128, and 256×256. The quantitative analysis results are presented in Tables 1 and 2. The experimental data demonstrate that the enhanced WNO model exhibits significant robustness across varying resolutions. Notably, the test errors for both the X-velocity component and the temperature field show minimal variation across different resolutions, thereby robustly validating the model's resolution invariance.

To rigorously evaluate the generalization capability of the enhanced WNO model, we performed extensive experiments under diverse initial conditions (e.g., varying velocity and temperature field distributions) and across a range of resolutions (from 64×64 to 256×256). By rigorously calculating the $L2$ error between the deep learning predictions and the ground truth, we quantitatively evaluate the performance of different models. The $L2$ error is calculated as follows:

$$L2_\text{error}(x_i, x_j) = \frac{\sqrt{\sum_{k=1}^{N} \left(\hat{u}(x_i, x_j) - u(x_i, x_j)\right)^2}}{\sqrt{\sum_{k=1}^{N} u(x_i, x_j)^2}}, \quad (26)$$

where i and j represent the spatial coordinates in 2D space, N is the total number of time steps in the testing dataset, $\hat{u}(x_i, x_j)$ denotes the prediction made by the deep learning model at coordinates (x_i, x_j), and $u(x_i, x_j)$ represents the corresponding ground truth.

The results indicate that the enhanced WNO model achieves superior generalization performance, accurately capturing the dynamic evolution of the flow field and temperature field, even under significant changes in initial conditions

or resolutions, without requiring additional retraining. This characteristic contrasts sharply with conventional deep learning models, which typically necessitate parameter fine-tuning or supplementary training to adapt to new data distributions when encountering different resolutions or initial conditions. In contrast, our enhanced WNO model, by leveraging its inherent operator learning capabilities, can seamlessly adapt to different resolutions and initial conditions while maintaining high predictive accuracy.

This advantage not only substantially reduces computational resource requirements and time costs but also significantly enhances the model's flexibility and practical utility in real-world applications. It enables the model to efficiently address complex and dynamic fluid dynamic simulation tasks. In conclusion, the enhanced WNO model has demonstrated exceptional adaptability and reliability in modeling complex multi-scale phenomena, thereby solidifying its position as an efficient and versatile tool for intermediate and advanced applications in the field of complex fluid dynamics simulation.

3.2. Two-dimensional turbulent Kolmogorov flow

3.2.1. Experimental setup and dataset

In this experiment, we evaluate the generalization performance of the enhanced wavelet neural operator model using the two-dimensional Kolmogorov flow dataset. The dataset, generated through direct numerical simulation, is downsampled to multiple resolutions, creating various input scenarios.

The dynamics of the Kolmogorov flow are governed by the incompressible Navier–Stokes equations, formulated as

$$\frac{\partial \omega(x,t)}{\partial t} + u(x,t)\cdot\nabla\omega(x,t) = \frac{1}{Re}\nabla^2\omega(x,t) + f(x), \quad (27)$$

where $\omega(x,t)$ represents the vorticity field, $u(x,t)$ denotes the velocity vector field, Re is the Reynolds number, and $f(x)$ is the spatially dependent forcing term, with $x = [x_1, x_2]$ representing the spatial coordinates. Periodic boundary conditions are applied in this study. The specific form of the forcing term for the two-dimensional Kolmogorov flow is given by

$$f(x) = -4\cos(4x_2) - 0.1\omega(x,t). \quad (28)$$

The additional drag force term $0.1\omega(x,t)$ is introduced to mitigate large-scale energy accumulation, thereby ensuring the statistical stability of the flow. The discretization grid is uniform, with a spatial resolution of 2048×2048. Data generated from direct numerical simulations are considered high-fidelity ground truth, which is utilized to assess the model's predictive performance. The dataset consists of 40 independent temporal sequences, each capturing the evolution of the flow field over 10 seconds with a temporal resolution of $\Delta t = 1/32$ second.

To rigorously evaluate the generalization capabilities of the enhanced WNO model, we systematically downsample the original high-resolution data to generate input scenarios at multiple resolutions. The high-fidelity simulation data serve as the benchmark reference for a thorough comparative evaluation. This innovative cross-resolution predictive experimental framework enables a systematic assessment of the model's multi-scale adaptive capabilities and robustness in handling resolution variations, while also facilitating an in-depth exploration of its generalization potential across diverse application domains. The experimental results provide reliable empirical evidence for model optimization and deployment.

3.2.2. Experimental results

Our initial evaluation of the enhanced WNO model was systematically conducted at two lower resolutions, 64×64 and 128×128, with a focused emphasis on its predictive capabilities for flow fields. The experimental results demonstrate that the model accurately captures the essential dynamic features of the flow field, exhibiting superior predictive performance, particularly in regions with significant gradient variations. Error analysis reveals that prediction errors are localized and minimal, underscoring the model's proficiency in reconstructing complex turbulent structures. While a marginal increase in errors is observed in areas of intense turbulence, the overall error levels remain remarkably low, further affirming the model's robustness and predictive accuracy. As illustrated in Fig. 6, the enhanced WNO model's flow field predictions at 128×128 resolution show high consistency with actual data, with error distributions predominantly concentrated in high-turbulence regions, aligning closely with theoretical expectations.

To further explore the scalability of the enhanced WNO model and its ability to resolve fine flow features, we increased the computational resolution to 256×256. Under these high-resolution conditions, the model demonstrates enhanced accuracy in resolving fine-scale structures within the flow field, showcasing significant advantages in capturing the evolutionary dynamics of the complex turbulence phenomenon. Although a slight increase in error magnitude persists in regions of intense turbulence, the overall error levels remain low, indicating that the enhanced WNO model maintains high prediction accuracy and numerical stability, even in more complex flow scenarios. As depicted in Fig. 7, the model successfully predicts flow field characteristics with precision at the 256×256 resolution, with error distribution patterns consistent with those observed at lower resolutions, primarily localized in high-turbulence regions. These results robustly validate the enhanced WNO model's capability to address complex flow field prediction challenges.

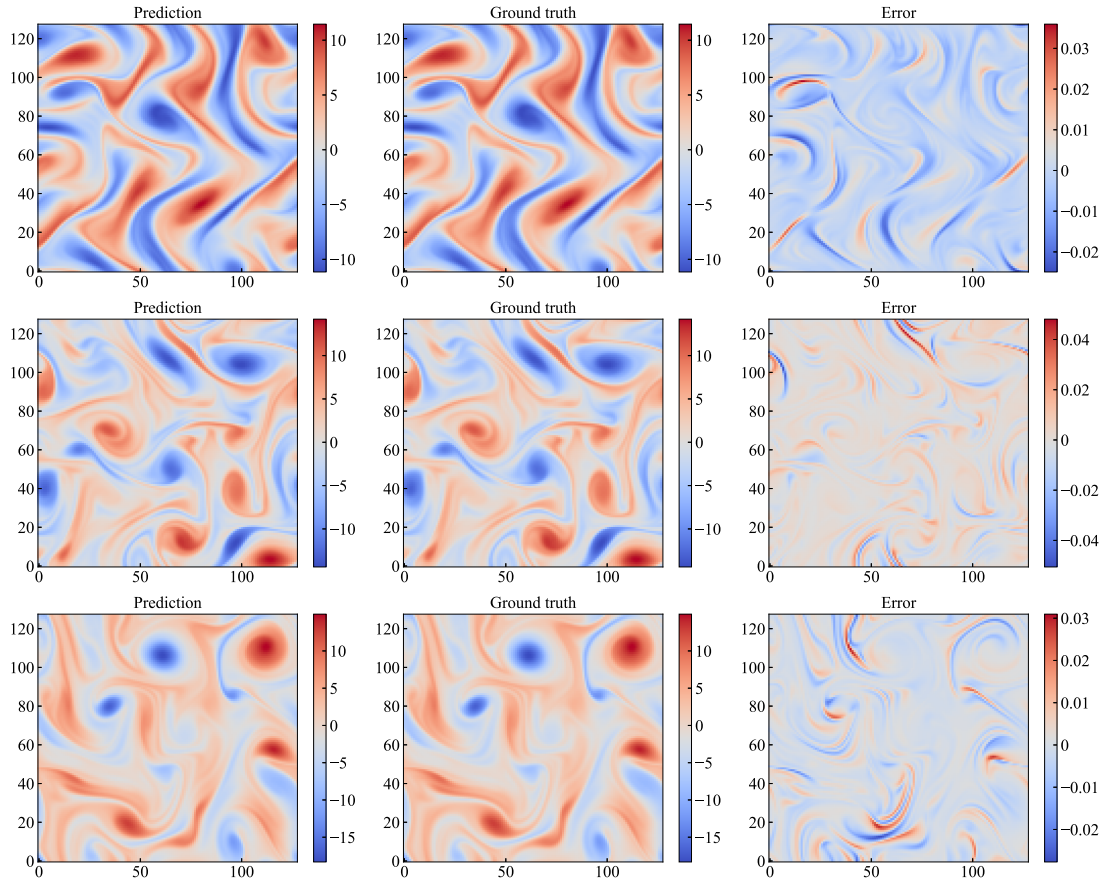


Fig. 6. Flow field predictions at 128×128 resolution: the enhanced WNO model (left column), true data (middle column), and error distribution (right column) at three different time steps.

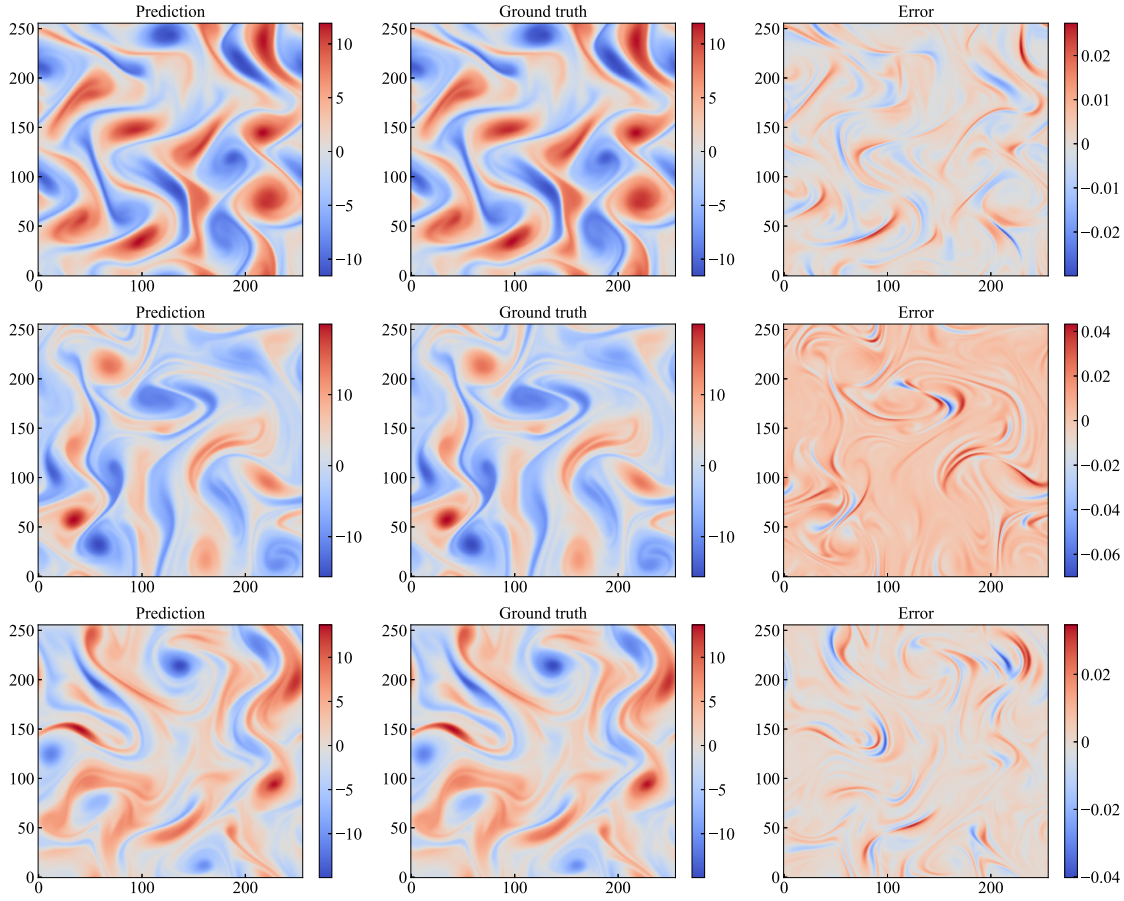


Fig. 7. Flow field predictions at 256×256 resolution: enhanced WNO model (left column), true data (middle column), and error distribution (right column) at three different time steps.

Table 3. Comparative analysis of $L2$ error metrics for two-dimensional turbulent Kolmogorov flow across different models at multiple resolutions: 64×64, 128×128, and 256×256.

Models	**64×64**	**128×128**	**256×256**
UNet	3.75×10^{-1}	6.42×10^{-1}	5.68×10^{-1}
ResNet	8.59×10^{-3}	9.67×10^{-3}	1.25×10^{-2}
FNO	6.94×10^{-4}	7.25×10^{-3}	5.59×10^{-3}
The enhanced WNO	$\mathbf{5.07 \times 10^{-4}}$	$\mathbf{9.96 \times 10^{-4}}$	$\mathbf{8.69 \times 10^{-4}}$

For a quantitative assessment, Table 3 provides a systematic comparison of the predictive performance of the enhanced WNO model against mainstream architectures such as UNet, ResNet, and FNO at resolutions of 64×64, 128×128, and 256×256. The experimental data reveal that the enhanced WNO model significantly outperforms the comparative models in turbulence prediction tasks, exhibiting consistently lower error levels. Notably, as the resolution increases, the enhanced WNO model maintains stable and low prediction errors, demonstrating its exceptional ability to capture complex multi-scale physical phenomena.

The comprehensive experimental results highlight that the enhanced WNO model maintains excellent prediction accuracy across varying resolution conditions, showcasing its superior generalization ability and efficient numerical computational performance. The model's exceptional performance not only validates its theoretical advantages but also underscores its broad application potential in fluid dynamic simulations, turbulence mechanism research, and other cutting-edge scientific domains requiring high-precision predictions. These findings provide innovative solutions for the numerical simulation of complex flow systems and hold significant implications for advancing research in related fields.

4. Conclusion

In this study, we developed the enhanced WNO model as an efficient data-driven method for studying complex flow dynamics, offering a viable alternative to traditional high-precision numerical simulations. The enhanced WNO model achieves high prediction accuracy, computational efficiency, and strong generalization capabilities. It accurately reproduces velocity and temperature fields in atmospheric turbulence, maintaining low error rates even at varying resolutions, and does not require retraining when initial conditions change, thereby greatly enhancing its practicality in dynamic, complex flow environments and reducing the computational costs associated with repeated model adjustments. In future work, we will extend the current two-dimensional framework to three-dimensional simulations, enabling the capture of richer and more intricate physical phenomena. Furthermore, we plan to integrate WNO with state-of-the-art generative AI models, such as transformers and diffusion models, to further improve spatial resolution and tackle inverse problems like parameter estimation in large-scale, long-duration simulations. In addition, we will explore transitioning from an offline to an online learning paradigm to enhance the model's real-time applicability. Overall, the WNO model offers a promising, efficient, and accurate simulation framework for advancing research in climate and atmospheric sciences, as well as other fields requiring high-fidelity, multiscale flow simulations, and we will continue to optimize and validate it to fully realize its potential as a versatile tool for modeling complex physical systems.

Acknowledgement

Project supported by the National Natural Science Foundation of China (Grant Nos. 42005003 and 41475094).

References

[1] Kajishima T and Taira K 2016 *Computational fluid dynamics: incompressible turbulent flows* (Springer)
[2] Piquet J 2013 *Turbulent flows: models and physics* (Springer Science & Business Media)
[3] Argyropoulos C D and Markatos N 2015 *Applied Mathematical Modelling* **39** 693
[4] Kadaverugu R, Sharma A, Matli C and Biniwale R 2019 *Asia-Pacific Journal of Atmospheric Sciences* **55** 539
[5] Van Heerwaarden C C, Van Stratum B J, Heus T, Gibbs J A, Fedorovich E and Mellado J P 2017 *Geoscientific Model Development* **10** 3145
[6] Chung D and Pullin D 2010 *Journal of Fluid Mechanics* **643** 279
[7] Sharfuddin A A M and Ladeinde F 2023 *AIAA Aviation 2023 Forum* p. 4415
[8] Ishihara T, Gotoh T and Kaneda Y 2009 *Annual Review of Fluid Mechanics* **41** 165
[9] Fox R O 2012 *Annual Review of Fluid Mechanics* **44** 47
[10] Lee M and Moser R D 2015 *Journal of Fluid Mechanics* **774** 395
[11] Tryggvason G, Scardovelli R and Zaleski S 2011 *Direct numerical simulations of gas–liquid multiphase flows* (Cambridge university press)
[12] Panchigar D, Kar K, Shukla S, Mathew R M, Chadha U and Selvaraj S K 2022 *Neural Computing and Applications* **34** 21677
[13] Guo Y, Cao X, Song J and Leng H 2024 *Chin. Phys. B* **33** 020203
[14] Guo Y, Cao X and Peng K 2023 *Commun. Theor. Phys.* **75** 095003
[15] Guo Y, Cao X, Liu B and Gao M 2020 *Applied Sciences* **10** 5917
[16] Kou J and Zhang W 2021 *Progress in Aerospace Sciences* **125** 100725
[17] Ladickỳ L, Jeong S, Solenthaler B, Pollefeys M and Gross M 2015 *ACM Transactions on Graphics (TOG)* **34** 1
[18] Mendez M A, Ianiro A, Noack B R and Brunton S L 2023 *Data-driven fluid mechanics: combining first principles and machine learning* (Cambridge University Press)
[19] Kochkov D, Smith J A, Alieva A, Wang Q, Brenner M P and Hoyer S 2021 *Proc. Natl. Acad. Sci. USA* **118** e2101784118
[20] Guo Y, Cao X, Song J, Leng H and Peng K 2023 *Physics of Fluids* **35** 106603
[21] Sousa P, Rodrigues C V and Afonso A 2024 *Computer Methods in Applied Mechanics and Engineering* **429** 117133
[22] Guo Y, Cao X, Zhou M, Leng H and Song J 2024 *Physics of Fluids* **36** 115110
[23] Kovachki N, Li Z, Liu B, Azizzadenesheli K, Bhattacharya K, Stuart A and Anandkumar A 2023 *Journal of Machine Learning Research* **24** 1
[24] Azizzadenesheli K, Kovachki N, Li Z, Liu-Schiaffini M, Kossaifi J and Anandkumar A 2024 *Nature Reviews Physics* **6** 320
[25] Li Z, Huang D Z, Liu B and Anandkumar A 2023 *Journal of Machine Learning Research* **24** 1
[26] Kovachki N, Lanthaler S and Mishra S 2021 *Journal of Machine Learning Research* **22** 1

[27] Zhang T, Li L, López-Marrero V, Lin M, Liu Y, Yang F, Yu K and Atif M 2024 *Journal of Advances in Modeling Earth Systems* **16** e2023MS003898
[28] Cao Q, Goswami S and Karniadakis G E 2024 *Nature Machine Intelligence* **6** 631
[29] Shih B, Peyvan A, Zhang Z and Karniadakis G E 2025 *Computer Methods in Applied Mechanics and Engineering* **434** 117560
[30] Niarchos V and Papageorgakis C 2024 *Phys. Rev. D* **110** 045020
[31] Tripura T and Chakraborty S 2023 *Computer Methods in Applied Mechanics and Engineering* **404** 115783
[32] Tripura T, Awasthi A, Roy S and Chakraborty S 2023 *Computer Methods and Programs in Biomedicine* **232** 107436
[33] Lu C, Liu Y and Niu S 2011 *Journal of Geophysical Research: Atmospheres* **116** 3740
[34] Lu C, Liu Y, Niu S, Krueger S and Wagner T 2013 *Journal of Geophysical Research: Atmospheres* **118** 185
[35] Gao Z, Liu Y, Li X and Lu C 2018 *Journal of Geophysical Research: Atmospheres* **123** 2194
[36] Schneiders L, Meinke M and Schröder W 2017 *Journal of Fluid Mechanics* **819** 188